

In the format provided by the authors and unedited.

Understanding the regional pattern of projected future changes in extreme precipitation

S. Pfahl^{1*}, P. A. O’Gorman² and E. M. Fischer¹

¹Institute for Atmospheric and Climate Science, ETH Zurich, 8092 Zurich, Switzerland. ²Department of Earth, Atmospheric and Planetary Sciences, Massachusetts Institute of Technology, Cambridge, Massachusetts 02139, USA. *e-mail: stephan.pfahl@env.ethz.ch

Tables

Table 1: CMIP5 models and corresponding number of ensemble members.

Model name	Number of members
ACCESS1-0	1
ACCESS1-3	1
bcc-csm1-1-m	1
BNU-ESM	1
CanESM2	5
CCSM4	1
CMCC-CESM	1
CMCC-CM	1
CMCC-CMS	1
CNRM-CM5	1
CSIRO-Mk3-6-0	1
FGOALS-g2	1
GFDL-ESM2M	1
IPSL-CM5A-LR	3
IPSL-CM5A-MR	1
IPSL-CM5B-LR	1
MIROC5	2
MIROC-ESM-CHEM	1
MPI-ESM-LR	3
MPI-ESM-MR	1
MRI-CGCM3	1
NorESM1-M	1

Supplementary Figures

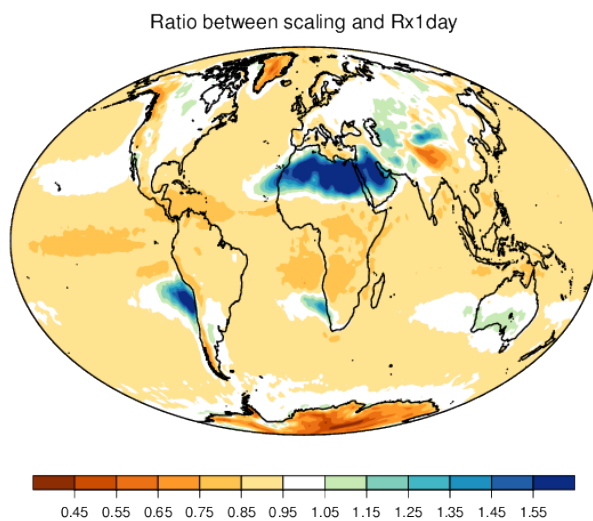


Figure S1: Ratio between present-day scaling and Rx1day. Ratio between multi-model mean precipitation extreme scaling and simulated precipitation extremes both averaged over the period 1981-2000.

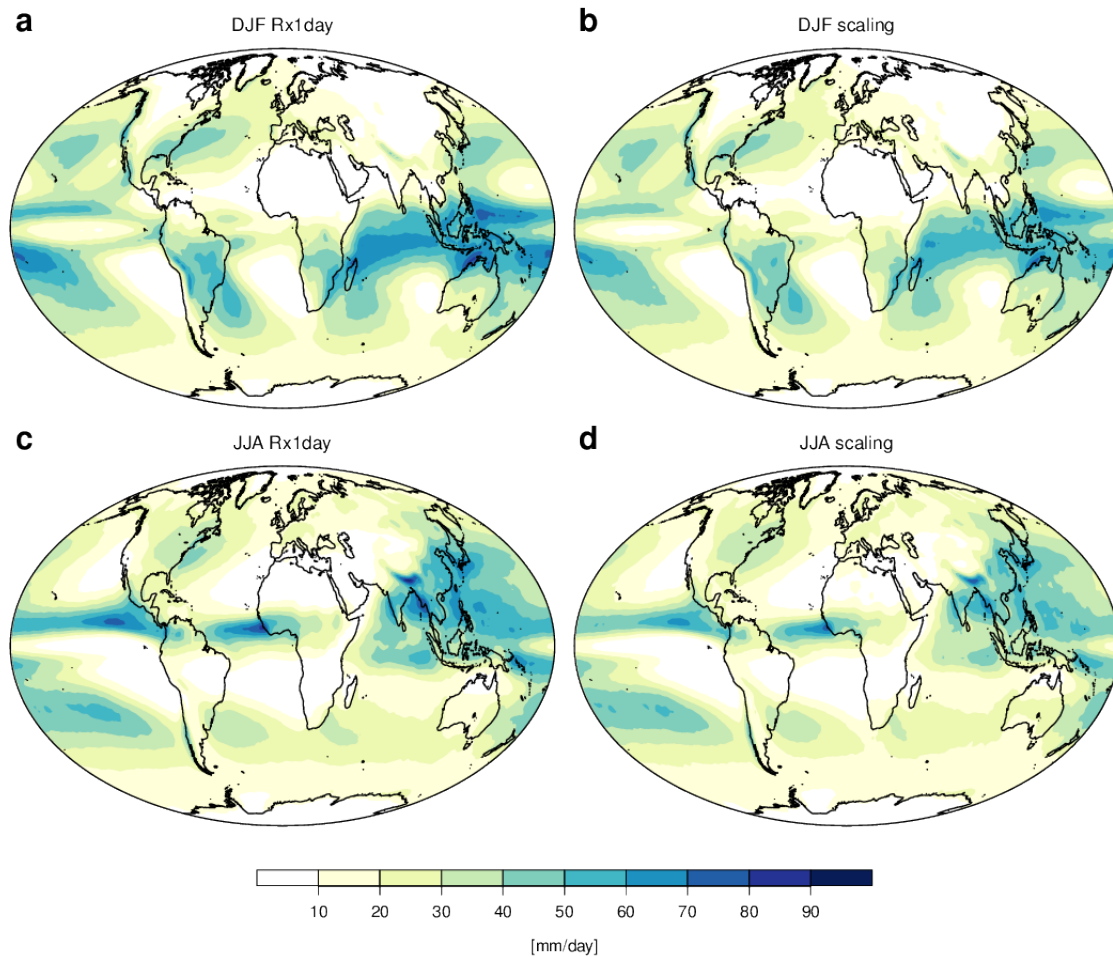


Figure S2. Present-day seasonal precipitation extremes and scaling. (a,c) Multi-model mean seasonal maximum precipitation and (b,d) precipitation extremes scaling (equation 1) for (a,b) December-February and (c,d) June-August, averaged over the period 1981-2000.

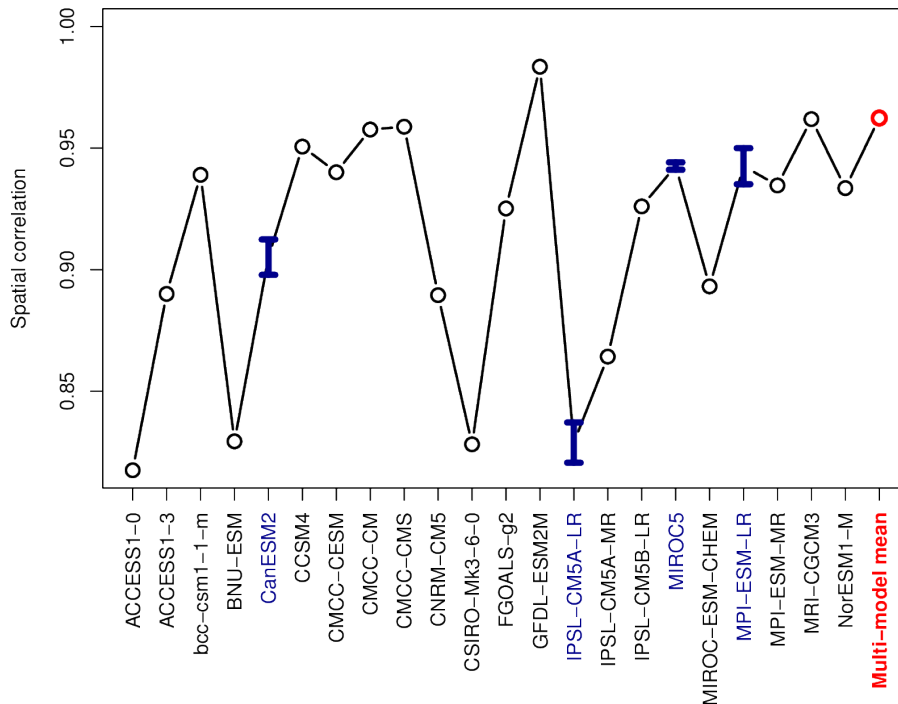


Figure S3. Agreement of spatial patterns of changes in precipitation extremes and scaling. Area-weighted spatial correlation coefficients between fractional changes in R_{x1} day and fractional changes in precipitation extremes scaling for individual models and the multi-model mean. Blue bars show the range of correlation coefficients obtained from different initial condition members of the same model. The width of these bars is relatively small compared to the inter-model spread, suggesting that the differences in correlation coefficients are mainly due to structural differences between the models (rather than internal variability).

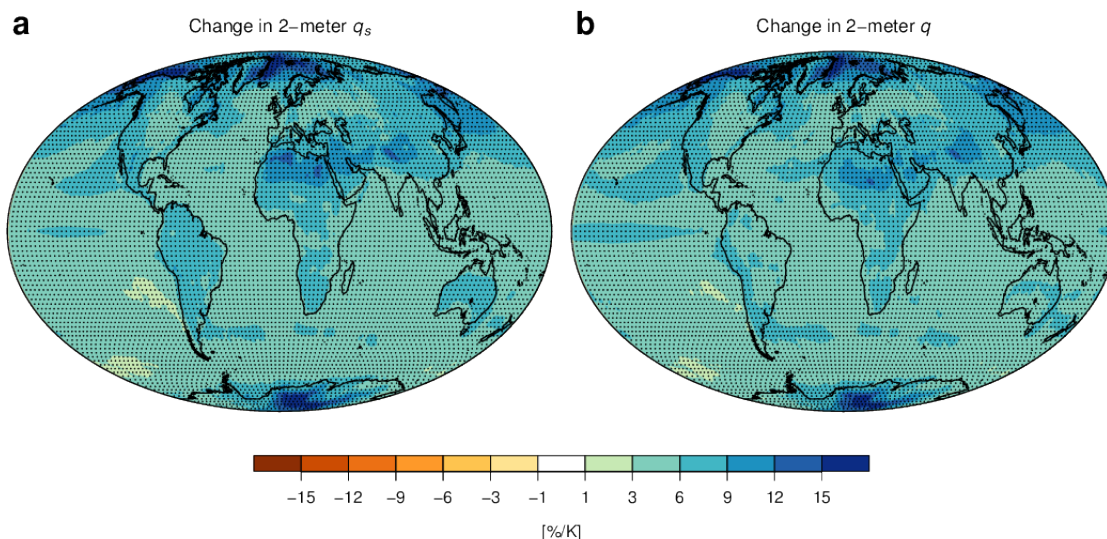


Figure S4: Changes in near-surface humidity. Multi-model mean fractional changes in (a) saturation specific humidity q_s and (b) actual specific humidity q at 2 meters above ground, both conditioned on the occurrence of extreme precipitation. Stippling indicates that at least 80% of the models agree on the sign of change. Note that only data from 16 (instead of 22) models was available for this analysis.

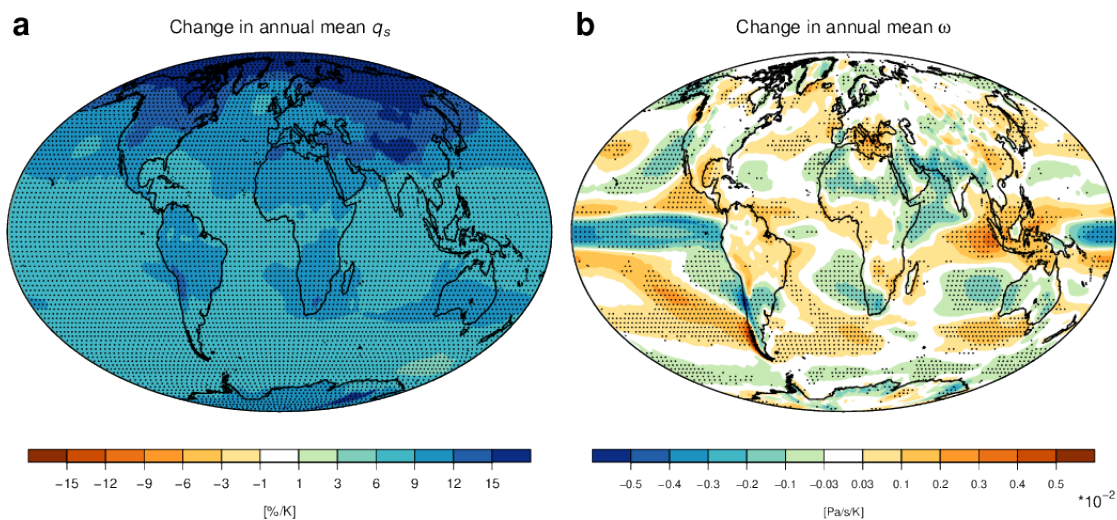


Figure S5. Changes in annual mean q_s and ω . Multi-model mean fractional changes in annual mean (a) vertically integrated saturation specific humidity q_s and (b) vertically averaged vertical velocity ω (with negative values indicating stronger ascent). Stippling indicates that at least 80% of the models agree on the sign of change.

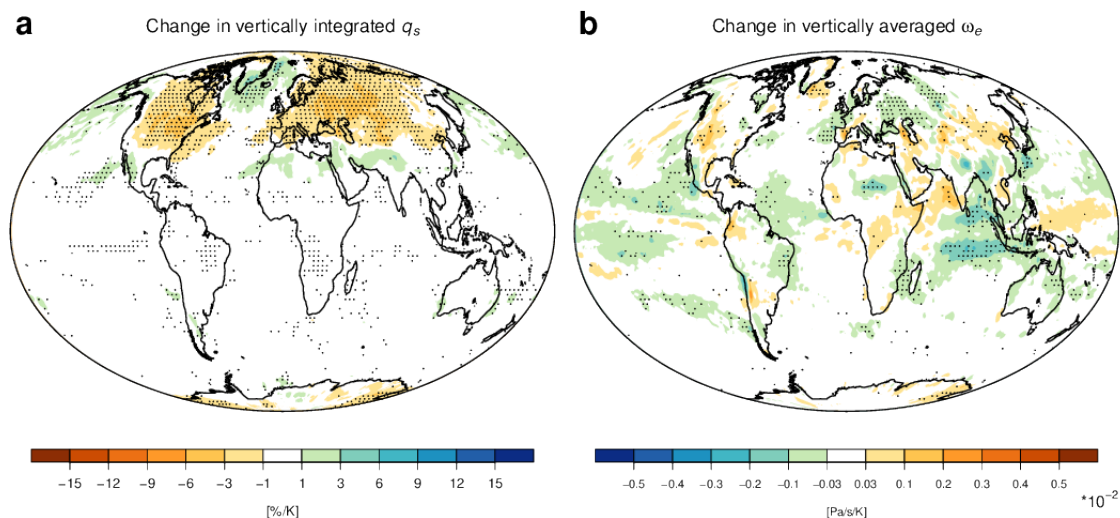


Figure S6. Changes in q_s and ω_e due to shifts in the seasonality of precipitation extremes. Multi-model mean fractional changes in climatological mean **(a)** vertically integrated saturation specific humidity q_s and **(b)** vertically averaged vertical velocity ω on the calendar day on which Rx1day occurs. These changes are derived from a linear regression for the period 1950-2100 in which the values of q_s and ω_e on the day of the annual maximum precipitation are replaced by the calendar day average values over the entire period. Stippling indicates that at least 80% of the models agree on the sign of change. The robust decrease in q_s in many continental regions indicates a shift in the seasonality of precipitation extremes towards smaller saturation humidity and thus lower temperature, and this may be interpreted as a shift to the cold season.

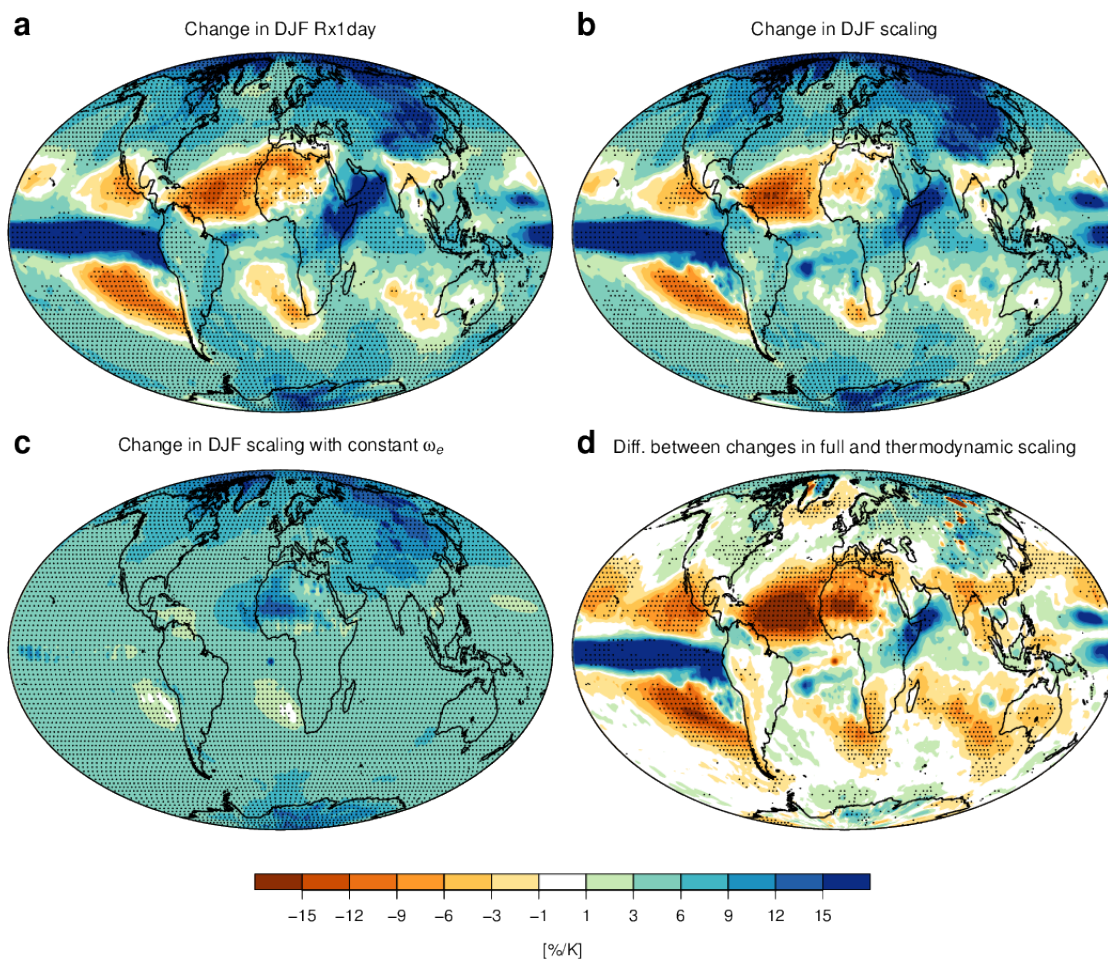


Figure S7. Scaling analysis for December-February (DJF). Multi-model mean fractional changes in (a) seasonal maximum precipitation, (b) full precipitation extremes scaling and (c) thermodynamic scaling in which the vertical velocity ω_e is kept constant. (d) Difference between changes in full scaling and changes in thermodynamic scaling (full minus thermodynamic). Stippling indicates that at least 80% of the models agree on the sign of change. A robust increase in DJF Rx1 day is found for 66% of the global land areas, and a robust decrease for 5%.

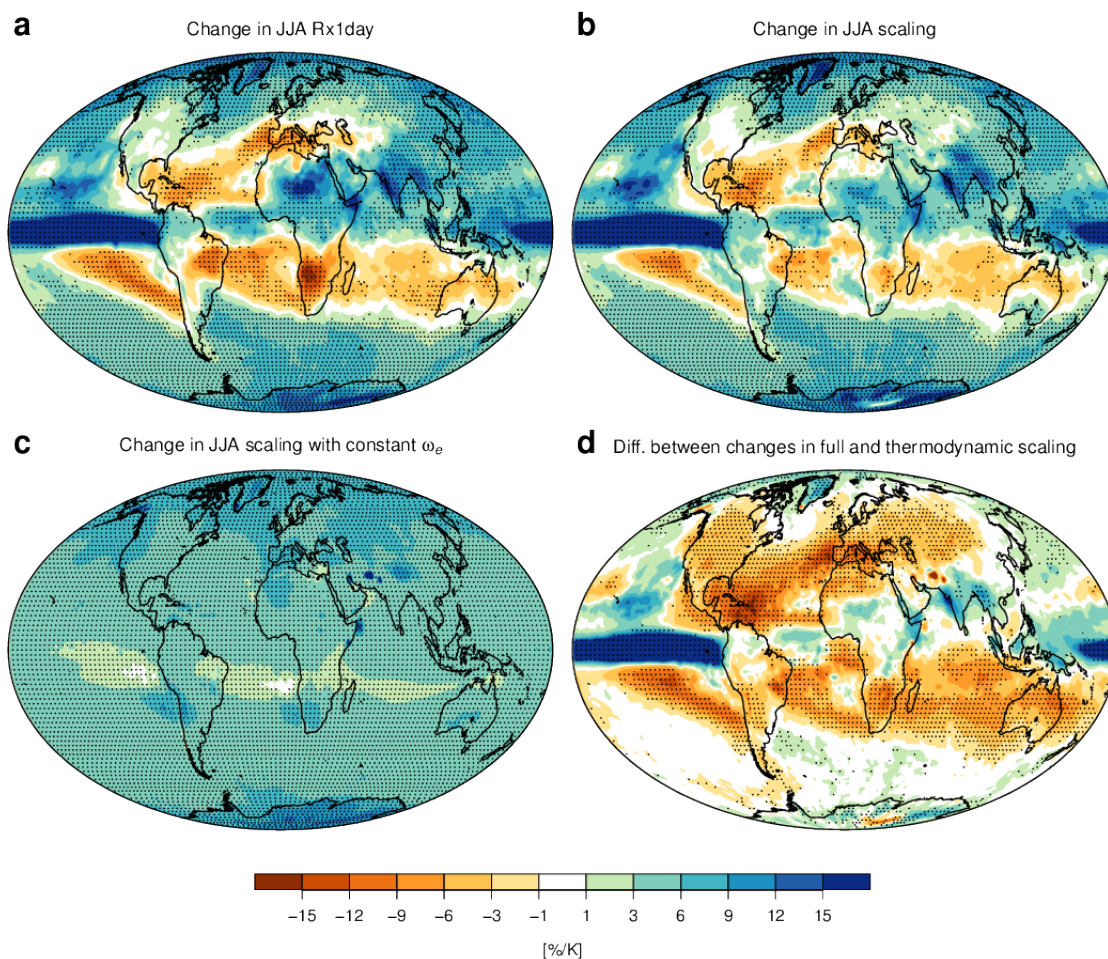


Figure S8. Scaling analysis for June-August (JJA). Multi-model mean fractional changes in (a) seasonal maximum precipitation, (b) full precipitation extremes scaling and (c) thermodynamic scaling in which the vertical velocity ω_e is kept constant. (d) Difference between changes in full scaling and changes in thermodynamic scaling (full minus thermodynamic). Stippling indicates that at least 80% of the models agree on the sign of change. A robust increase in JJA Rx1day is found for 47% of the global land areas, and a robust decrease for 6%.

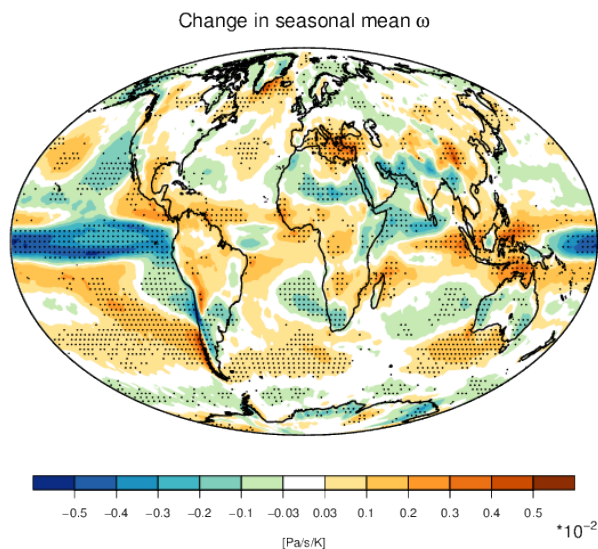


Figure S9. Changes in seasonal mean ω . Multi-model mean fractional changes in seasonal mean vertically averaged vertical velocity ω in the season (DJF, MAM, JJA or SON) in which the precipitation extremes occur most often at the respective location (with negative values indicating stronger ascent). Stippling indicates that at least 80% of the models agree on the sign of change.

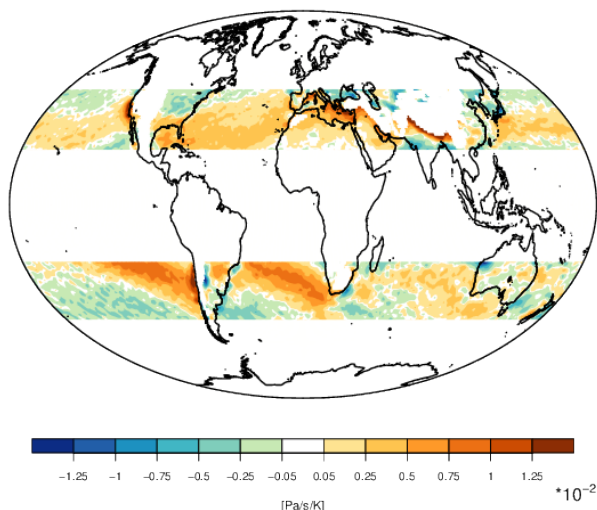
Anticipated change in ω_e due to Hadley cell expansion

Figure S10. Anticipated change in ω_e due to Hadley cell expansion. Change in the vertically averaged vertical velocity ω_e conditioned on the occurrence of extreme precipitation obtained from an artificial poleward shift of the present-day multi-model mean pattern of ω_e (see Fig. S11b) by 0.2° per K of multi-model mean global warming in the Northern Hemisphere and 0.32° per K in the Southern Hemisphere. This poleward shift mimics the poleward expansion of the Hadley cells as simulated by CMIP5 models²⁰. The field is masked in regions where the topography exceeds 1000 m as well as poleward of 45° and equatorward of 22° in each hemisphere. Note the different colour scale compared to Fig. 3d. This anticipated expansion explains the pattern of the simulated change in ω_e (see Fig. 3d) in the South Pacific, South Atlantic, eastern North Atlantic, Indian Ocean and Mediterranean region. The magnitude of the change is underestimated, which indicates that other factors are also important, or that the circulations associated with extreme precipitation shift poleward at a faster rate than the annual mean edge of the Hadley cells.

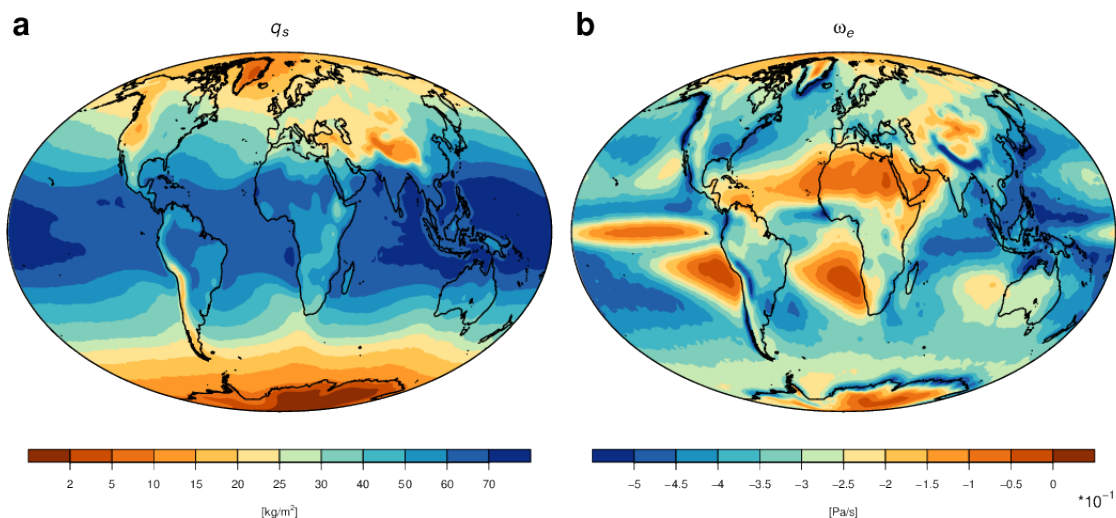


Figure S11. Present-day q_s and ω_e . (a) Multi-model mean vertically integrated saturation specific humidity q_s and (b) vertically averaged vertical velocity ω_e conditioned on the occurrence of extreme precipitation, averaged over the period 1981-2000.

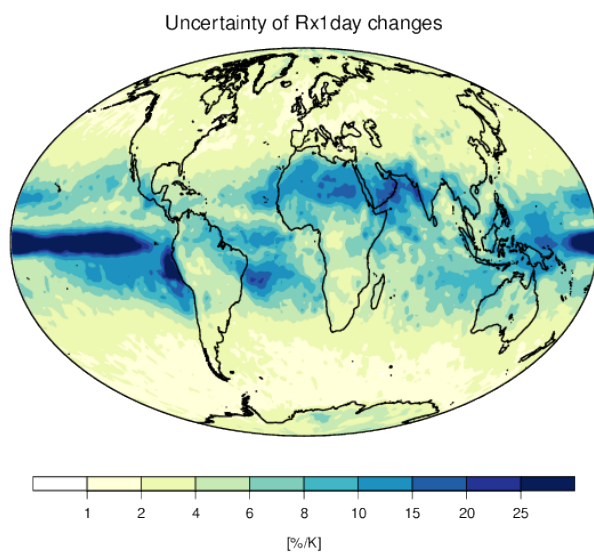


Figure S12. Uncertainty of changes in precipitation extremes. Absolute uncertainty of fractional changes in Rx1 day, quantified as the standard deviation of the regression coefficients across models. Note the non-linear scale.

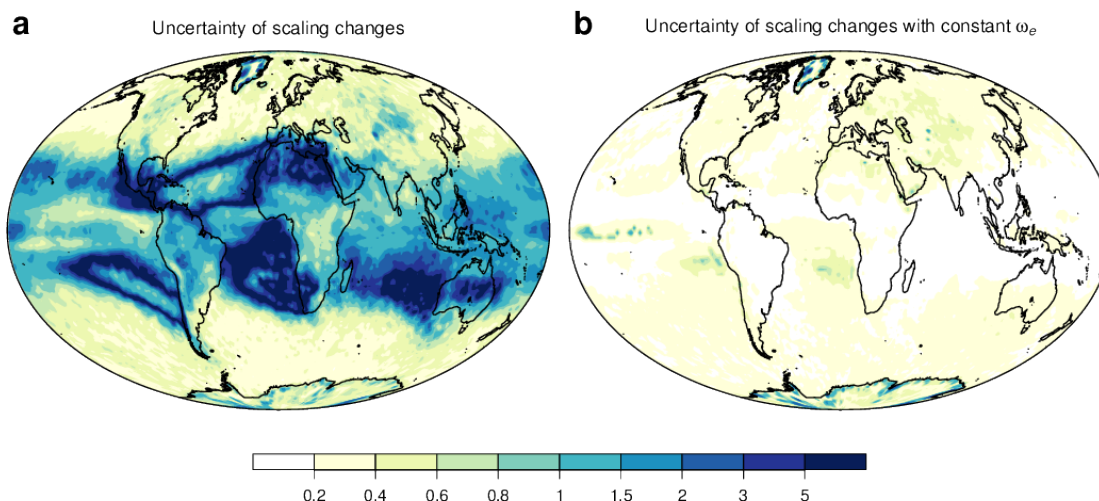


Figure S13. Relative uncertainty of changes in full and thermodynamic scaling.

Relative uncertainty of (a) fractional changes in full precipitation extremes scaling and (b) fractional changes in thermodynamic scaling with constant vertical velocity ω_e , quantified as the ratio of the standard deviation of the regression coefficients across models and the absolute value of the multi-model mean fractional change. Note the non-linear scale.

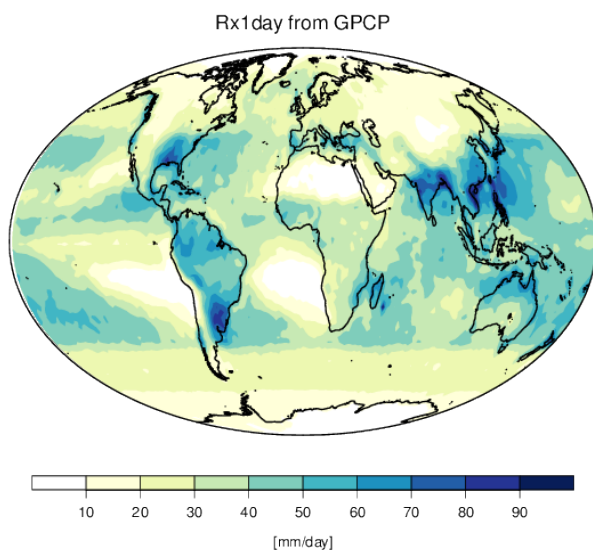


Figure S14. Rx1day from observations. Annual maximum precipitation from GPCP observations³³, averaged over the period 1996-2014.

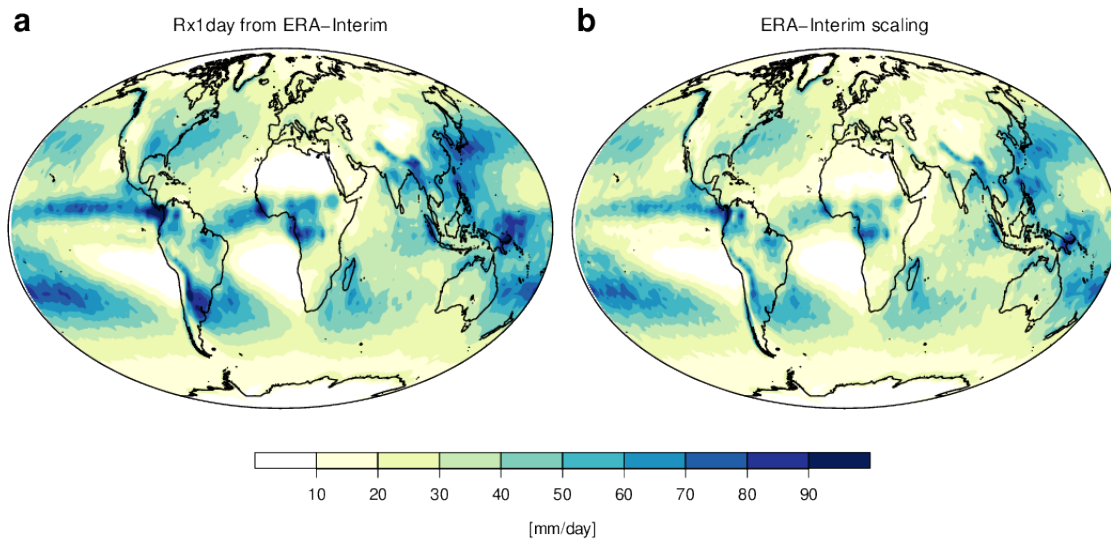


Figure S15. Rx1day and scaling from reanalysis data. (a) Annual maximum precipitation and (b) precipitation extremes scaling (equation 1) from ERA-Interim reanalysis data³⁶, both averaged over the period 1979-2015.